Yang *et al.*
Intelligent Marine Technology and Systems (2025) 3:13
https://doi.org/10.1007/s44295-025-00063-6

imts Intelligent Marine Technology and Systems

RESEARCH PAPER Open Access

A simple approach to measuring upper ocean light quality using an underwater camera

Xin Yang[1], Xiaolong Yu[1,2*], Gong Lin[1], Yongchao Wang[3] and Zhongping Lee[1]

Abstract

Solar radiation is the fundamental driving force of the Earth's system. In the upper water column, interactions such as absorption and scattering by water constituents decrease light intensity (photon quantity) and alter light quality (spectral distribution of photons). Although changes in solar intensity have been extensively studied over the years, variations in light quality with depth have received comparatively little scholarly attention. This dearth of research may be due to the lack of simple and cost-effective instruments for measuring light quality, unlike commercial instruments available for measuring solar intensity. In this study, we present a simple approach that uses an underwater camera and a diffuser to measure light quality, represented by the hue angle (HA) of the downwelling irradiance. Our results reveal that the HA from this simple, low-cost device aligns closely with measurements from an expensive hyperspectral radiometer across various water types, ranging from oceanic to coastal waters ($R^2 = 0.94$, mean absolute percentage difference = 1.64%). The widespread adoption of this approach could significantly enhance our understanding of the impact of solar radiation on the biogeochemical processes in aquatic environments.

Keywords Ocean color, Light quality, Hue angle, Underwater camera, Upper ocean

1 Introduction

Light is a critical factor that regulates the growth of marine phytoplankton, with the vertical distribution of underwater light fields playing a pivotal role in modulating their vertical zonation and primary productivity (Kirk 2011). Therefore, exploring the impacts of underwater light fields on phytoplankton's ecological and physiological functions has become a key focus in modern marine science (MacIntyre et al. 2002; Stomp et al. 2004). Many studies have investigated the impact of light on phytoplankton growth through light intensity, such as photosynthetically active radiation (PAR; Sathyendranath et al. 1989; Alver et al. 2014; Dutkiewicz et al. 2019). Other studies have found that insufficient light could suppress photosynthetic activity, whereas excessive light density may induce photoinhibition or cellular damage (Behrenfeld and Falkowski 1997; Xie et al. 2015). As a result, phytoplankton exhibit a photoacclimation mechanism to adapt to varying light intensities (Six et al. 2007). As the efficiency of phytoplankton photosynthesis varies significantly across different light wavelengths, light quality, which represents the spectral information of solar radiation at different wavelengths, can also affect phytoplankton growth. For example, under the same intensity, red light (620–750 nm) contributes markedly less to photosynthesis than blue-green wavelengths (450–550 nm) due to its rapid attenuation in shallow layers, while blue light (380–500 nm) can penetrate the deeper parts of the ocean, becoming the dominant driver of photosynthesis in deeper euphotic zones (Hintz et al. 2021). However, existing studies that have evaluated phytoplankton responses to light conditions have mainly focused on

*Correspondence:
Xiaolong Yu
xlyu@xmu.edu.cn
[1] State Key Laboratory of Marine Environmental Science, College of Ocean and Earth Sciences, Xiamen University, Xiamen 361005, China
[2] National Observation and Research Station for the Taiwan Strait Marine Ecosystem, Xiamen University, Zhangzhou 363400, China
[3] Tianjin Research Institute for Water Transport Engineering, National Engineering Research Center of Port Hydraulic Construction Technology, Tianjin 300456, China

light intensity metrics. In comparison, the impacts of light quality on the physiological and ecological functions of phytoplankton have rarely been explored.

To characterize the vertical distribution of light quality, Lee et al. (2022) employed the hue angle (HA, in degrees) of the downwelling irradiance (E_d, in W/m^2/nm), enabling them to quantify light quality variations in the upper water column using a simple index. By definition, HA represents the relative proportions of the red, green, and blue (RGB) tristimulus values in the chromaticity space (Wyszecki and Stiles 2000). In particular, HA has emerged as a new optical property for water quality monitoring. Over the years, the HA of surface water has been demonstrated as a more robust alternative to the Forel-Ule index (FUI; Bonney 1892; Wernand and van der Woerd 2010); therefore, it has been widely used for water quality monitoring (Lehmann et al. 2018; Shen et al. 2019; Wang et al. 2020). Furthermore, HA measurements from RGB photos or composited images, especially when combined with machine-learning methods, can further enhance the capability of water quality monitoring (Malthus et al. 2020; Xiao et al. 2022).

At present, hyperspectral radiometers, such as the HyperOCR of Seabird Scientific, are the primary instruments used to measure hyperspectral E_d and subsequently estimate the HA of E_d (i.e., light quality). However, these instruments are costly, thereby limiting their broad applications in measuring underwater light quality across different aquatic environments. To address this limitation, in the present study, we developed a cost-effective and easy-to-deploy approach by integrating a GoPro camera with an optical diffuser. This simple 'device' captures underwater RGB photos and obtains water HA at varying depths. The subsequent sections will provide a comprehensive description of the deployment of this device, data quality control, and calibration procedures for the proposed approach. Such an approach ensures that accurate and consistent HA measurements can be obtained from the GoPro and diffuser, as well as the HyperOCR.

2 Data and methods

2.1 Field measurements

This study utilized measurements from two field surveys conducted in the northern South China Sea and the western Pacific Ocean. The sampling locations of all measurements are presented in Fig. 1, and their corresponding geographic coordinates are listed in Table 1. The northern South China Sea represents a typical coastal environment with high spatial heterogeneity in terms of water quality, characterized by chlorophyll-*a* concentrations ranging from 0.1 to 5 mg/m^3. In comparison, the western Pacific Ocean features open-ocean conditions, with lower chlorophyll-*a* concentrations (ca. 0.1 mg/m^3) and relatively less temporal variability. Data from the western Pacific were collected during a winter cruise (December 2020–January 2021), resulting in three stations with nine high-quality vertical profiles after quality control (see

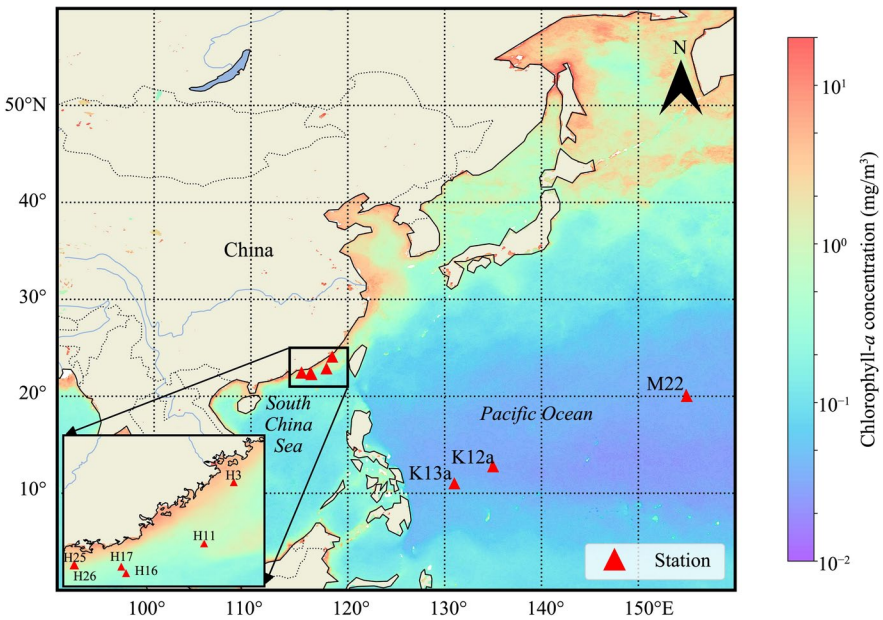

Fig. 1 Sampling locations of all the field measurements. The background represents data on the annually averaged chlorophyll-*a* concentration in 2023 from MODIS-Aqua, which were acquired through the NASA OceanColor website (https://oceancolor.gsfc.nasa.gov/)

Table 1 Station names with their geographic coordinates and sampling times

Station name	Longitude (E)	Latitude (N)	Sampling time (UTC + 8 h)
K12a	135°00′	12°45′	2021.01.24 06:48
K13a	131°00′	11°00′	2021.01.26 07:08
M22	155°00′	20°00′	2021.01.11 08:37
H3	118°24′	24°00′	2023.06.06 15:48
H11	117°48′	22°51′	2023.06.07 14:43
H16	116°15′	22°15′	2023.06.08 08:36
H17	116°09′	22°23′	2023.06.08 10:35
H25	115°13′	22°24′	2023.06.09 10:05
H26	115°12′	22°24′	2023.06.09 12:05

Section 2.2). The northern South China Sea dataset was collected in June 2023, comprising six stations and 10 vertical profiles after quality control.

In this study, the hyperspectral E_d data were measured using a HyperOCR irradiance radiometer mounted on the free-falling Profiler II system (Sea-Bird Scientific, Fig. 2a). Additionally, a GoPro camera with an optical diffuser attached to its lens (Fig. 2c) was housed in a waterproof casing and mounted on the Profiler II system to take zenith-view images simultaneously with the E_d measurements (Fig. 2b). The HyperOCR recorded 3–4 hyperspectral E_d data per second. Ancillary information, including time, depth, and tilt angle, was simultaneously recorded with E_d data. Notably, to simultaneously measure the downwelling irradiance above the sea surface (E_s), an additional HyperOCR irradiance radiometer was mounted on the deck. The GoPro camera was configured to automatically capture photos every 5 s, during which the acquisition times were also recorded. Typically, due to the presence of sunlight (photos not shown here), a strong light spot with saturated brightness appears in the center of the GoPro photos when taking zenith-view photos underwater. Therefore, we employed the semiopaque white diffusing glass from Edmund Optics and attached it to the GoPro lens to diffuse the light field in the water column. The selected diffuser had a size of 25 mm × 25 mm, a thickness of 1.25 mm, and a transmission efficiency of ca. 30% in the visible band. The size of such a diffuser is perfectly suited to cover the GoPro camera lens (Fig. 2c). We used two different GoPro cameras during the coastal (GoPro Hero 6) and the open ocean (GoPro Hero 8) cruises.

2.2 Data matching and processing

The overall data processing workflow is summarized in Fig. 3, which particularly illustrates the parallel handling of the hyperspectral E_d and GoPro-derived HA for subsequent data analysis. The workflow comprised four steps, including (1) data processing, (2) calculation of HA, (3) quality control, and (4) data match and regression analysis. These steps were designed to ensure spatiotemporal alignment, enhance data

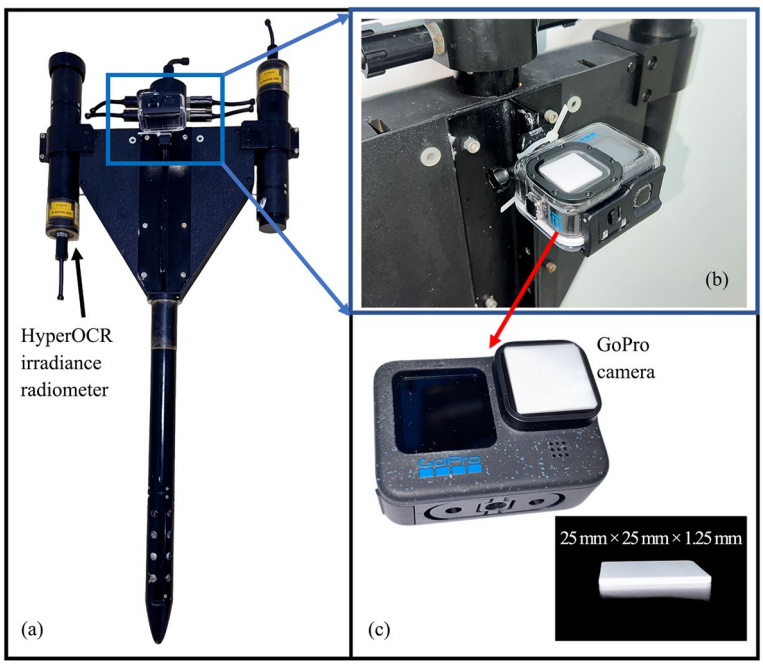

Fig. 2 Illustration of the concurrent hue angle (HA) measurement system with the (**a**) Profiler II and (**b** and **c**) GoPro camera

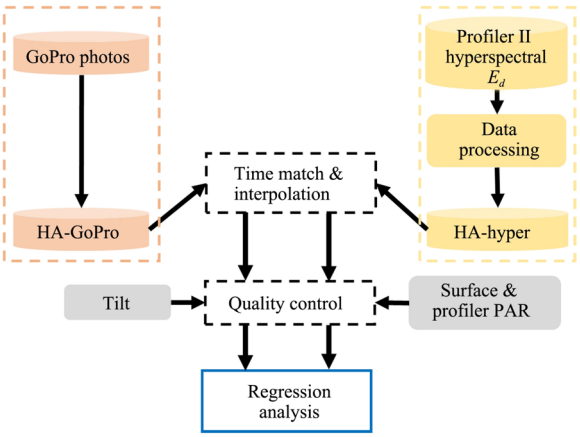

Fig. 3 Flowchart showing the processing and matching procedure for the two measuring systems

quality, and establish robust relationships between the camera- and hyperspectral-derived HAs.

2.3 Data processing and quality control

To obtain Level 4 data products, raw data were collected using the Profiler II instrument and processed using the ProSoft software (v. 7.7.19 b2). The output Level 4 product included hyperspectral measurements of E_d and E_s, instrument tilt angle, and corresponding PAR data at various times and depths. RGB photos were directly obtained from the GoPro camera.

Quality control was performed based on three criteria: the instrument tilt angle, consistency in the time series of the surface PAR, and the vertical distribution of the underwater PAR. Given that large instrument tilt angles (> 3°) result in deviations in E_d measurements from the true values, all E_d measurements with tilt angles exceeding 3° were discarded. Rapid fluctuations in the surface PAR indicate short-term environmental changes (e.g., cloud movement), which introduce temporal alignment uncertainties when interpolating the E_d-measured HA to the GoPro-measured HA. This resulted from the differences in the sampling frequency when the timestamps of the two devices were left unsynchronized. In addition, to ensure that all measurements were conducted under a relatively stable dynamic environment, the vertical profile of PAR, which typically followed an exponential decrease with depth, was also checked for each deployment. Thus, the hyperspectral E_d measurements were retained only for conditions in which the surface PAR was stable throughout the deployment period (5–8 min), and the PAR profiles exhibited an exponentially decreasing trend.

2.4 Calculation of the HA and regression analysis

The formula used by Lee et al. (2022) was adopted to calculate the HA from hyperspectral E_d to quantify light quality variations in the upper water column. For the hyperspectral E_d data measured by Profiler II, the RGB tristimulus values were first computed by integrating $E_d(\lambda)$ over the visible spectrum (400–700 nm), weighted by the CIE standard color-matching functions $\bar{r}(\lambda)$, $\bar{g}(\lambda)$, and $\bar{b}(\lambda)$ (Novoa et al. 2015; Wang et al. 2015):

$$\begin{cases} R = \int_{400}^{700} E_d(\lambda)\bar{r}(\lambda)\mathrm{d}\lambda \\ G = \int_{400}^{700} E_d(\lambda)\bar{g}(\lambda)\mathrm{d}\lambda \cdot \\ B = \int_{400}^{700} E_d(\lambda)\bar{b}(\lambda)\mathrm{d}\lambda \end{cases} \tag{1}$$

Next, the chromaticity coordinates (x, y) were derived from the following normalized RGB values:

$$\begin{cases} x = \frac{R}{R+G+B} \\ y = \frac{G}{R+G+B} \end{cases}. \tag{2}$$

The HA (in °) was then calculated following Lee et al. (2022):

$$HA = 90 - \mathrm{atan2}(y - 0.333, x - 0.333)\frac{180}{\pi}. \tag{3}$$

As for the raw photos acquired by the GoPro camera, these were read using the Matlab function *imread*, resulting in a three-dimensional (3D) array of 3000 × 4000 ×3 RGB values of the photo stored in each of the 3000 ×4000 matrices (i.e., corresponding to the photo resolution). Then, the RGB values were extracted from each matrix and averaged across the entire photo. As a preliminary quality control measure, the outermost 200 pixels of each matrix were excluded from calculating the mean RGB value due to potential edge effects. The obtained mean RGB values of each photo were then used to calculate the chromaticity coordinates (x, y) and HA following Eqs. (2) and (3), respectively. Due to the difference in the sampling frequency (Section 2.1), the GoPro-derived HA (i.e., HA-GoPro) values were temporally interpolated to match those from the hyperspectral E_d (i.e., HA-hyper) based on the timestamp. Finally, a quadratic expression was used to relate HA-GoPro to HA-hyper, and the model coefficients were obtained through least squares fitting.

2.5 Statistical metrics

Here, four metrics were employed to evaluate the performance of the calibrated model: the coefficient of determination (R^2), mean absolute percentage difference (*MAPD*), root mean squared difference (*RMSD*), and

mean absolute difference (*MAD*). Their corresponding mathematical formulations are expressed as follows:

$$R^2 = 1 - \frac{\sum_{i=1}^{n}\left(\widehat{y}_i - y_i\right)^2}{\sum_{i=1}^{n}\left(\bar{y} - y_i\right)^2}, \tag{4}$$

$$MAPD = \frac{1}{n}\sum_{i=1}^{n}\left|\frac{\widehat{y}_i - y_i}{y_i}\right| \times 100\%, \tag{5}$$

$$RMSD = \sqrt{\frac{1}{n}\sum_{i=1}^{n}\left(\widehat{y}_i - y_i\right)^2}, \tag{6}$$

$$MAD = \frac{1}{n}\sum_{i=1}^{n}\left|\widehat{y}_i - y_i\right|, \tag{7}$$

where y_i and $\widehat{y}_i$ denote the HA-hyper (i.e., the reference HA value) and the converted HA from HA-GoPro through the quadratic expression, respectively, $\bar{y}$ is the mean value of HA-hyper, and n represents the number of data points.

3 Results and discussion

3.1 Results for the oceanic waters

Through the data quality procedure, measurements at three stations (K12a, K13a, and M22-3, respectively; Table 1) in the western Pacific Ocean were retained for subsequent analysis. At each station, Profiler II was deployed three times, yielding nine vertical profiles of the hyperspectral E_d and GoPro photos. As an example, the third profile from station K12a (denoted K12a-3) was used here to illustrate the vertical distributions of E_d and the corresponding RGB photos at different depths (Fig. 4). Notably, the data from the surface layer (i.e., within 2 m) were removed due to large instrument tilt angles during the quality control procedure.

As shown in Fig. 4a, E_d in the red domain attenuated rapidly with depth, decreasing to near zero at 30 m. In contrast, blue light exhibited slower attenuation, with residual spectral detected at depths of 70 m. The corresponding RGB photos revealed a gradual shift in watercolor from green and light blue at the surface ocean to dark blue at greater depths (Fig. 4b), as only blue light was retained at these depths. After matching the HA-GoPro to the HA-hyper based on the timestamp, we obtained 186 pairs of HA measurements from the two devices for all nine deployments. Next, we employed a quadratic polynomial expression to calibrate the nonlinear relationship between HA-GoPro and HA-hyper (Fig. 5a). The calibrated model is expressed as follows:

$$y = -0.0287x^2 + 11.18x - 853.37, \tag{8}$$

where x and y represent HA-GoPro and HA-hyper, respectively.

As shown in Fig. 5a, a strong agreement was observed between the two HA measurements over a large range of HA, where the HAs measured from the GoPro and Hyperspectral E_d cameras ranged within 170°–200° and 215°–240°, respectively. Despite the difference in the measured HA range between the two devices, almost all the matched HA-GoPro and HA-hyper data fell within the 95% confidence intervals (CI) of the calibrated model, suggesting high confidence in the developed model. The robustness of the calibrated model was further illustrated

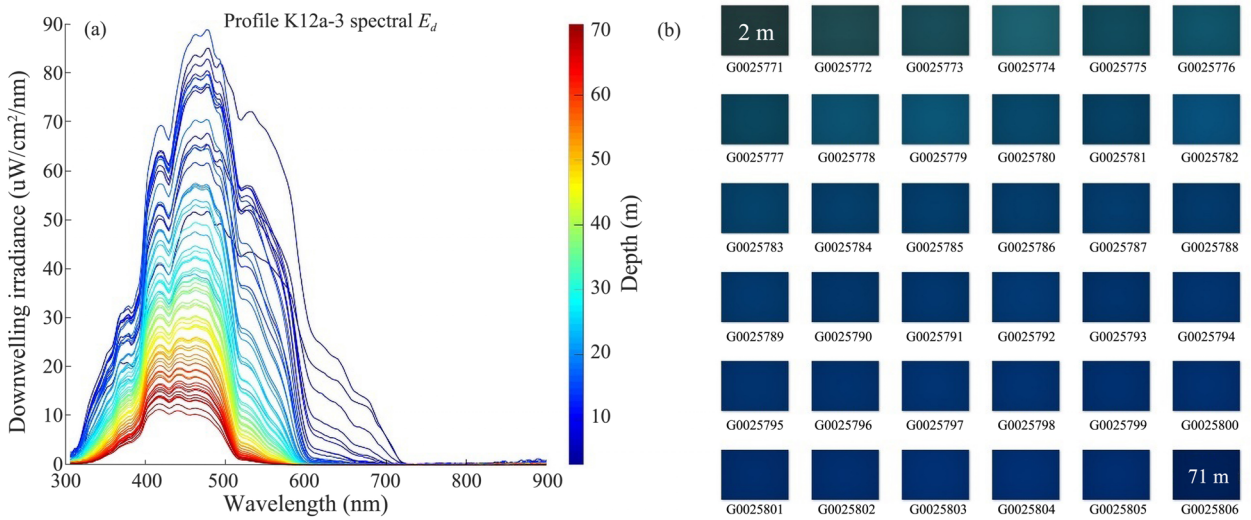

Fig. 4 (**a**) Depth profiles of the downwelling irradiance at station K12a-3 and (**b**) zenith-view photos captured by the GoPro camera with a diffuser at increasing depths

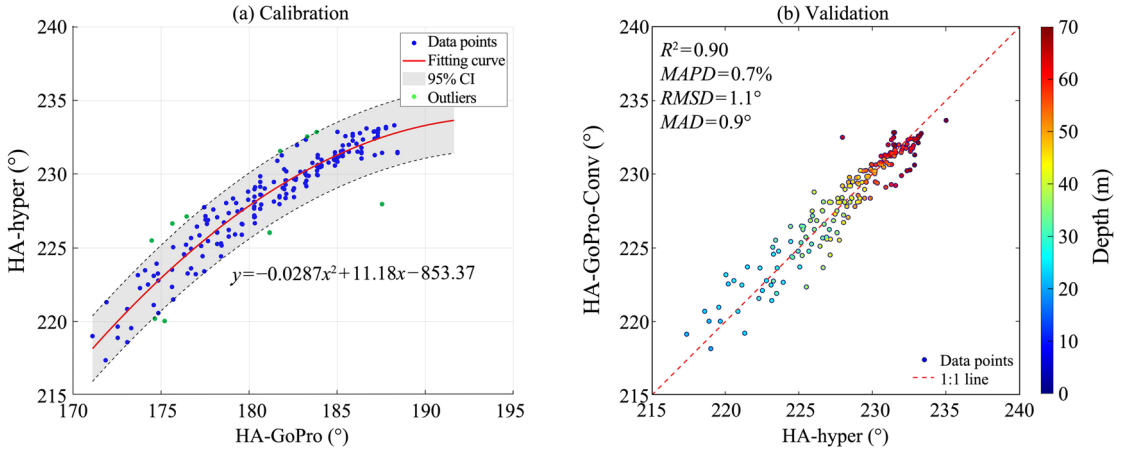

Fig. 5 The relationship between HAs measured from hyperspectral E_d and GoPro Camera for oceanic water samples. **a** The calibrated relationship between HA-GoPro and HA-hyper, with the red line representing the fitting curve and the gray shading indicating the 95% confidence intervals (CI). The green points are marked as outliers exceeding the 95% CI. **b** Validation of the converted HA from HA-GoPro against the reference HA-hyper

by the statistical results in Fig. 5b, in which the converted HA from HA-GoPro aligned very well with HA-hyper, as most data points were distributed closely to the 1:1 line. Furthermore, the high R^2 values of 0.90 and the low errors in the converted HA ($MAPD = 0.7\%$, $RMSD = 1.1°$, $MAD = 0.9°$) suggested good agreement between the converted HA and the reference HA-hyper. Therefore, these metrics confirm the model's robustness in oceanic waters, suggesting the possibility of obtaining highly accurate HA measurements from a GoPro camera with a diffuser.

3.2 Results for the coastal waters

For the coastal cruise, measurements at six stations (H3, H11, H16, H17, H25, and H26, respectively; see Table 1) in the northern South China Sea, with 10 vertical profiles, were retained after the quality control procedure. For example, the hyperspectral E_d measurements and corresponding GoPro photos collected from the second profile at station H3 (denoted H3-2) are presented here. The variations in the spectral E_d and RGB photos with increasing depth are shown in Figs. 6a and 6b, respectively.

As shown in Fig. 6, the decrease in E_d was more pronounced in the coastal stations than in the oceanic stations, which can be attributed to the greater optical complexity and higher concentrations of water constituents in the coastal waters. For example, the chlorophyll-*a* concentration at H3-2 was 3.3 mg/m^3 compared to 0.04 mg/m^3 at the oceanic station K12a-3 (Fig. 4). More importantly, in comparison to the overall blue color in the oceanic waters, the color of the coastal waters at H3-2 changed from light green to deep green with increasing depths. Consequently, HA for all the measurements in coastal waters spanned from 130° to 170° and from 160°

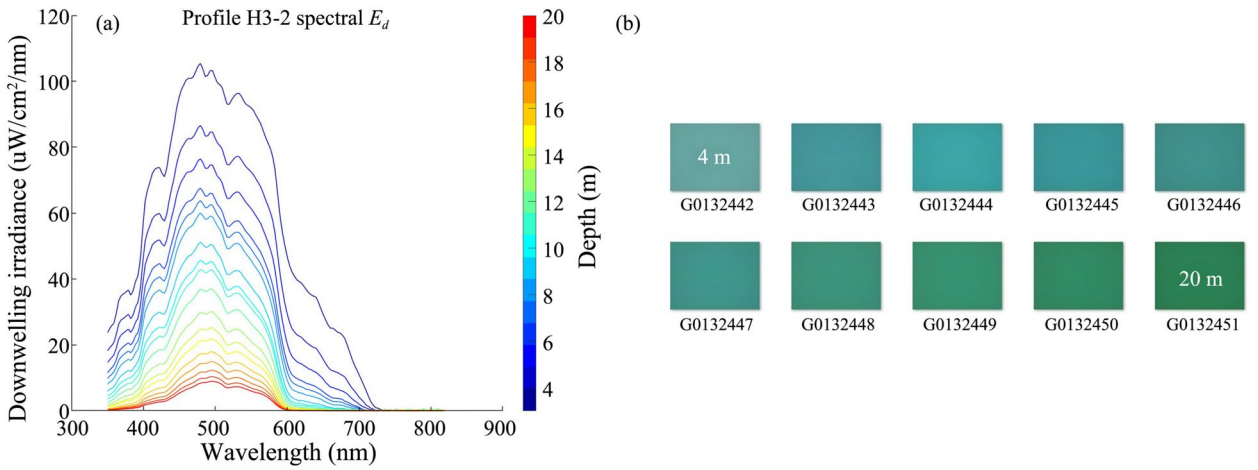

Fig. 6 Same as in Fig. 4 but for the coastal station H3-2

to 220° for HA-GoPro and HA-hyper, respectively. Similar to the approach applied to the oceanic water measurements, we used a quadratic regression model to relate HA-GoPro to HA-hyper for coastal waters (Fig. 7a). The fitted quadratic equation is expressed as follows:

$$y = 0.0346x^2 - 8.946x + 749.97, \quad (9)$$

where x and y represent HA-GoPro and HA-hyper, respectively.

As shown in Fig. 7a, the relationship between HA-GoPro and HA-hyper appeared less robust than that in oceanic waters. Although most data points fell within the 95% CI, the data points were much more scattered than those of the oceanic measurements (Fig. 5). The validation results in Fig. 7b also confirmed the relatively degraded performance of the calibrated model in coastal oceans, with lower R^2 values (= 0.75) and higher errors of the converted HA from HA-GoPro (*MAPD* = 3.0%, *RMSD* = 7.2°, *MAD* = 5.8°) compared to that in oceanic waters. The relatively larger uncertainties for the calibrated model could be attributed to the effects of the complex water constituents in the coastal waters, such as colored dissolved organic matter and suspended sediments. The GoPro camera, which is equivalent to a three-channel broadband radiometer, may not be able to accurately capture the nonlinear influence of complex water constituents on the hyperspectral E_d and the subsequent HA in the dynamic coastal oceans. As such, extensive measurements may be required to further evaluate the capability of our proposed approach in measuring HA in coastal waters. Nevertheless, generally speaking, a *MAPD* value of 3.0% for the converted HA from HA-GoPro is acceptable for providing reasonable HA measurements using the proposed device. Future enhancements or refinements of the calibrated model for coastal oceans will require additional simultaneous field measurements using hyperspectral E_d and GoPro photos across diverse water types.

3.3 Relationship between HA-GoPro and HA-hyper for all data collected in oceanic and coastal waters

Using all the data collected in this study, we recalibrated the model to convert HA-GoPro to HA-hyper, enabling us to obtain the relationship between HA-GoPro and HA-hyper across all water types. The calibration and validation of the converted model for HA-GoPro using data collected from oceanic and coastal waters are shown in Fig. 8. In this aspect, HA-GoPro exhibited a broader range, spanning from 130° to 190°, whereas HA-hyper ranged from 160° to 240° (Fig. 8a). The calibrated model is also fitted through a quadratic function and is expressed as follows:

$$y = -0.0062x^2 + 3.291x - 164.939, \quad (10)$$

where x and y represent HA-GoPro and HA-hyper, respectively.

As shown in Fig. 8 an overall satisfying relationship can be observed between the converted HA from HA-GoPro and HA-hyper for the combined dataset, with approximately 89% of the data points falling within the 95% CI. The error metrics also demonstrated the overall good agreement (R^2 = 0.94, *MAPD* = 1.6%, *RMSD* = 4.9°, *MAD* = 3.3°) between the converted HA from GoPro and HA-hyper. Unsurprisingly, the data points deviating from the fitting curve, particularly the outliers (green points in Fig. 8a), originated from measurements in coastal waters. Nevertheless, these error statistics, with an *MAPD* of 1.6%, confirmed the robustness of the proposed simple approach in obtaining relatively high-accuracy measurements of HA across oceanic and coastal waters.

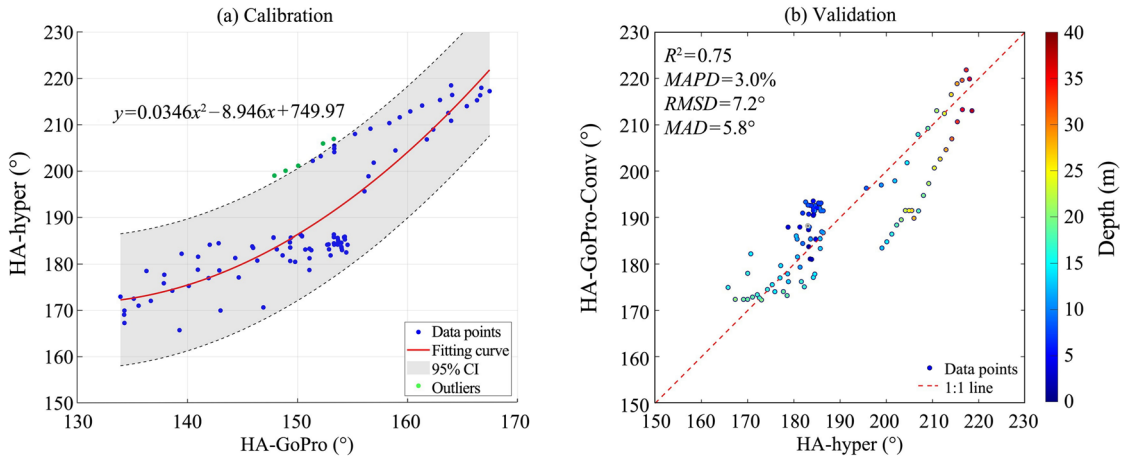

Fig. 7 Same as in Fig. 5, but for data collected from coastal waters

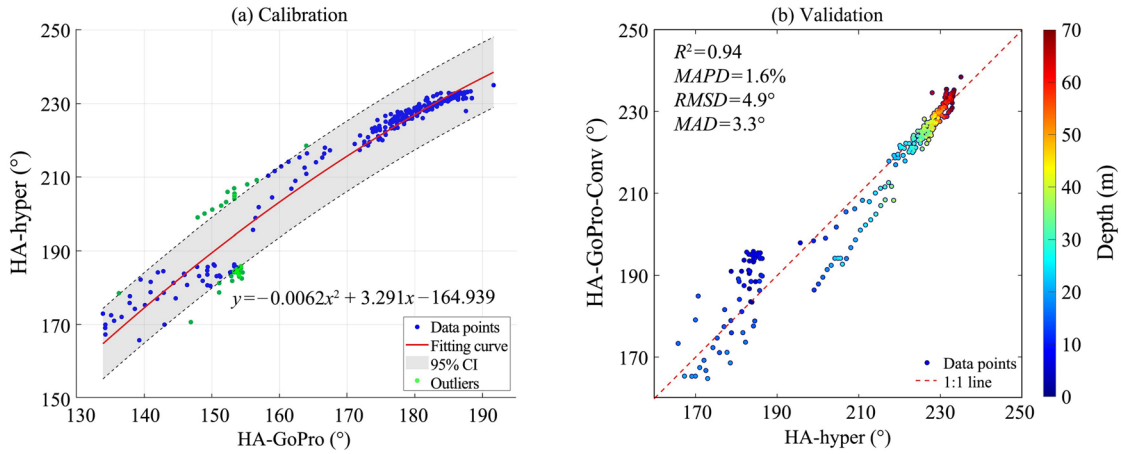

Fig. 8 Same as in Fig. 5, but for all data collected in this study, including oceanic and coastal water measurements

3.4 Limitations and perspectives

Despite the overall satisfactory conversion from HA-GoPro to HA-hyper, there is still room for further improvement in the HA measurements using GoPro. For example, the relatively large deviations observed for measurements from coastal waters may require further optimization. On the one hand, more concurrent measurements across different types of coastal waters and varying light conditions are necessary to expand the calibration dataset, thus enhancing data representativeness and the model's applicability. Ensuring data representativeness in the calibration dataset could be an ideal prerequisite for obtaining high-accuracy HA measurements by GoPro across different water types. On the other hand, because the Profiler II and GoPro were not precisely synchronized, interpolating between hyperspectral E_d and GoPro photos based on timestamps may have resulted in uncertainties, especially for scenarios in which HA changed rapidly within 5 s (i.e., the sampling frequency of GoPro). Thus, future experiments must ensure the exact synchronization between Profiler II and GoPro prior to deployment.

Finally, the use of different GoPro cameras (i.e., GoPro Hero 6 in the South China Sea cruise and GoPro Hero 8 in the western Pacific cruise) may have led to some systematic bias when developing a model based on data collected from the two cruises (Fig. 8). Fundamentally, the color captured by each camera could be influenced by various factors, such as the focus and depth of field, camera hardware configurations (camera and lens properties), image processing algorithm (adjusting contrast, saturation, and sharpness), setting in white balance and exposure, and spectral response of the RGB channel. However, these factors could differ largely from camera to camera, especially for cameras manufactured by different companies. Thus, using calibration coefficients for each camera would be necessary. To minimize the potential impact of camera settings on the color of underwater photos, we recommend calibrating the photos taken in the auto mode for the HA measurement. Such an approach facilitates the direct application of the calibrated coefficients by other researchers. Our subsequent efforts will focus on providing detailed calibration coefficients and establishing a standard calibration protocol for various commercial underwater cameras, including different models of GoPro and DJI Osmo Action.

With high confidence in the HA measured by our proposed device, further efforts will focus on expanding the measurements of HA profiles across the global ocean. To conveniently collect HA measurements, this simple device equipped with calibrated coefficients to convert to HA can be easily mounted on other underwater instruments, such as a conductivity-temperature-depth sampler. In addition to providing insights into the distributions of underwater light quality, the extensive HA measurements across the global ocean can also be used to investigate their impacts on phytoplankton biomass and productivity. Doing so could provide valuable insights into the regulatory mechanisms of light quality on the physiological and ecological functions of phytoplankton.

Furthermore, similar to the many successful applications of water quality monitoring using RGB images captured by digital cameras (Gao et al. 2020, 2022), future efforts could focus on correlating the measured HA with the bio-optical properties found in the water column. For example, the color of the GoPro-captured photos exhibited a monotonic shift from light blue to dark blue with increasing depth in oceanic waters (see Fig. 4b), while shifts from cyan to green occurred in coastal waters as depth increased. These distinct and

region-dependent color changes, along with vertical variations, can be fundamentally attributed to differences in the optical properties of the waterbody in these two regions, such as the inherent optical properties and the diffuse attenuation coefficient (K_d, in m^{-1}). Therefore, it may be possible to estimate these optical properties from the GoPro-measured HA when extensive matched measurements are available. Such estimations can be conducted using regression or machine-learning approaches.

4 Conclusions

In this study, we proposed a simple approach/device to measure the light quality of the upper ocean, quantified by the HA of the downwelling irradiance, using a GoPro camera and a diffuser. The HA measured using this simple device aligned very well with that of an expensive hyperspectral radiometer for measurements collected in oceanic and coastal waters. Despite the relatively larger uncertainties in the coastal waters, the overall uncertainty in the measured HA by GoPro was only 1.6% in terms of *MAPD* across all the data collected in this study. Such high accuracy provides confidence in using this simple device for taking HA measurements in the upper ocean.

Furthermore, the simplicity and portability of the proposed device make it ideal for convenient HA profiling measurements across various bodies of water. With additional HA measurements, it would be possible to explore the impacts of light quality on the physiological and ecological functions of phytoplankton. We anticipate that the HA, along with light density, temperature, and nutrients, will become a key factor used by the scientific community to investigate the regulatory mechanisms of phytoplankton growth.

Acknowledgements
This work was supported in part by the National Key Research and Development Program of China (Grant Nos. 2022YFC3104900, 2022YFC3104901), and the National Natural Science Foundation of China (Grant No. 42376173). The support from the crew of the *R/V TKK* during the western Pacific Ocean cruise is greatly appreciated. The collection of data and samples was supported by the NSFC Shiptime Sharing Project (Grant Nos. 42249904, 42249906).

Additional information
Edited by: Wenwen Chen.

Authors' contributions
Xin Yang: data processing and analysis, original draft, and manuscript revision. Xiaolong Yu: research design, data collection, manuscript editing, and revision. Gong Lin and Yongchao Wang: data collection and processing. Zhongping Lee: research design and manuscript revision.

Data Availability
The data is available from the corresponding author upon reasonable request.

Declarations

Ethics approval and consent to participate
Not applicable.

Consent for publication
Informed consent for publication was obtained from all participants.

Competing interests
The authors declare that they have no competing interests. Zhongping Lee is one of the Editorial Board Members, but he was not involved in the journal's review of or decision related to this manuscript.

Received: 4 March 2025 Revised: 3 April 2025 Accepted: 25 April 2025
Published online: 06 May 2025

References

Alver MO, Hancke K, Sakshaug E, Slagstad D (2014) A spectrally-resolved light propagation model for aquatic systems: steps toward parameterizing primary production. J Mar Syst 130:134–146. https://doi.org/10.1016/j.jmarsys.2012.03.007

Behrenfeld MJ, Falkowski PG (1997) A consumer's guide to phytoplankton primary productivity models. Limnol Oceanogr 42(7):1479–1491. https://doi.org/10.4319/lo.1997.42.7.1479

Bonney TG (1892) Le Léman: monographie limnologique. Nature 47:5–6. https://doi.org/10.1038/047005a0

Dutkiewicz S, Hickman AE, Jahn O, Henson S, Beaulieu C, Monier E (2019) Ocean colour signature of climate change. Nat Commun 10(1):578. https://doi.org/10.1038/s41467-019-08457-x

Gao M, Li JS, Wang SL, Zhang FF, Yan K, Yin ZY et al (2022) Smartphone-camera-based water reflectance measurement and typical water quality parameter inversion. Remote Sens 14(6):1371. https://doi.org/10.3390/rs14061371

Gao M, Li JS, Zhang FF, Wang SL, Xie Y, Yin ZY et al (2020) Measurement of water leaving reflectance using a digital camera based on multiple reflectance reference cards. Sensors 20(22):6580. https://doi.org/10.3390/s20226580

Hintz NH, Zeising M, Striebel M (2021) Changes in spectral quality of underwater light alter phytoplankton community composition. Limnol Oceanogr 66(9):3327–3337. https://doi.org/10.1002/lno.11882

Kirk JTO (2011) Light and photosynthesis in aquatic ecosystems. Cambridge University Press, Cambridge and New York

Lee ZP, Shang SL, Li YH, Luis K, Dai MH, Wang YC (2022) Three-dimensional variation in light quality in the upper water column revealed with a single parameter. IEEE Trans Geosci Remote Sens 60:1–10. https://doi.org/10.1109/TGRS.2021.3093014

Lehmann MK, Nguyen U, Allan M, van der Woerd HJ (2018) Colour classification of 1486 lakes across a wide range of optical water types. Remote Sens 10(8):1273. https://doi.org/10.3390/rs10081273

MacIntyre HL, Kana TM, Anning T, Geider RJ (2002) Photoacclimation of photosynthesis irradiance response curves and photosynthetic pigments in microalgae and cyanobacteria. J Phycol 38(1):17–38. https://doi.org/10.1046/j.1529-8817.2002.00094.x

Malthus TJ, Ohmsen R, van der Woerd HJ (2020) An evaluation of citizen science smartphone apps for inland water quality assessment. Remote Sens 12(10):1578. https://doi.org/10.3390/rs12101578

Novoa S, Wernand M, van der Woerd HJ (2015) WACODI: a generic algorithm to derive the intrinsic color of natural waters from digital images. Limnol Oceanogr Meth 13(12):697–711. https://doi.org/10.1002/lom3.10059

Sathyendranath S, Platt T, Caverhill CM, Warnock RE, Lewis MR (1989) Remote sensing of oceanic primary production: computations using a spectral model. Deep-Sea Res Part I-Oceanogr Res Pap 36(3):431–453. https://doi.org/10.1016/0198-0149(89)90046-0

Shen Q, Yao Y, Li JS, Zhang FF, Wang SL, Wu YH et al (2019) A CIE color purity algorithm to detect black and odorous water in urban rivers using high-resolution multispectral remote sensing images. IEEE Trans Geosci Remote Sens 57:6577–6590. https://doi.org/10.1109/TGRS.2019.2907283

Six C, Finkel ZV, Irwin AJ, Campbell DA (2007) Light variability illuminates niche-partitioning among marine picocyanobacteria. PLoS One 2(12):e1341. https://doi.org/10.1371/journal.pone.0001341

Stomp M, Huisman J, de Jongh F, Veraart AJ, Gerla D, Rijkeboer M et al (2004) Adaptive divergence in pigment composition promotes phytoplankton biodiversity. Nature 432(7013):104–107. https://doi.org/10.1038/nature03044

Wang SL, Li JS, Shen Q, Zhang B, Zhang FF, Lu ZY (2015) MODIS-based radiometric color extraction and classification of inland water with the Forel-Ule scale: a case study of Lake Taihu. IEEE J Sel Top Appl Earth Observ Remote Sens 8(2):907–918. https://doi.org/10.1109/JSTARS.2014.2360564

Wang SL, Li JS, Zhang B, Lee ZP, Spyrakos E, Feng L et al (2020) Changes of water clarity in large lakes and reservoirs across China observed from long-term MODIS. Remote Sens Environ 247:111949. https://doi.org/10.1016/j.rse.2020.111949

Wernand MR, van der Woerd HJ (2010) Spectral analysis of the Forel-Ule ocean colour comparator scale. J Eur Opt Soc-Rapid Publ 5:10014s. https://doi.org/10.2971/jeos.2010.10014s

Wyszecki G, Stiles WS (2000) Color science: concepts and methods, quantitative data, and formulae. John Wiley & Sons, New York

Xiao Y, Guo YH, Yin GD, Zhang X, Shi Y, Hao FH et al (2022) UAV multispectral image-based urban river water quality monitoring using stacked ensemble machine learning algorithms–a case study of the Zhanghe River. China Remote Sens 14(14):3272. https://doi.org/10.3390/rs14143272

Xie YY, Huang BQ, Lin LZ, Laws EA, Wang L, Shang SL et al (2015) Photosynthetic parameters in the northern South China Sea in relation to phytoplankton community structure. J Geophys Res-Oceans 120(6):4187–4204. https://doi.org/10.1002/2014JC010415

Publisher's Note